Vortex supercurrent inversion by frequency-symmetry conversion of Cooper pairs

Soma Yoshida,[1] Shu-Ichiro Suzuki ●,[2,1,*] and Yukio Tanaka[1]

[1]*Department of Applied Physics, Nagoya University, Nagoya 464-8603, Japan*
[2]*MESA+ Institute for Nanotechnology, University of Twente, 7500 AE Enschede, The Netherlands*

We theoretically demonstrate that the vortex supercurrent can be reversed by the frequency-symmetry conversion among Cooper pairs by surface Andreev bound states. The surface of a three-dimensional superconductor pierced by a flux quantum is considered. We compare the vortex supercurrents near the surface of the spin-singlet s-wave and spin-triplet p_z-wave superconductors using quasiclassical Eilenberger theory, where the surface is perpendicular to the z direction. We demonstrate that the vortex supercurrent near the surface of a p_z-wave superconductor is reversed compared to those far from the surface, whereas that of an s-wave superconductor is not. The splitting of the zero-energy states caused by the interference of the surface Andreev bound states and Caroli-de Gennes-Matricon modes is demonstrated.

I. INTRODUCTION

The magnetic flux penetrating a type-II superconductor (SC) is quantized (i.e., quantum vortices) since a macroscopic wave function describing the Cooper pair condensate must be single valued. The phase winding around the vortex results in a shielding current that localizes the magnetic field at the core. This is how type-II SCs maintain the perfect diamagnetism even in a magnetic field.

However, recent experiments confirmed the existence of *paramagnetic* superconducting states [1,2]. Applying a low-energy muon spin relaxation (μSR) technique for superconducting bilayer systems, the local magnetic field was larger than that of the applied magnetic field. This local enhancement is well understood in terms of odd-frequency (odd-ω) Cooper pairs [3–5]. The pair density of odd-ω pairs was *effectively negative* [6], meaning that odd-ω pairs show the opposite response to perturbations compared with the well-known even-ω pairs [1,2,6–12]: Novel odd-ω pairings attract external fields.

Odd-ω pairs appear in inhomogeneous systems [13–22]. In addition to $U(1)$-symmetry breaking, the inhomogeneity locally breaks the inversion symmetry and causes parity mixing of the Cooper pairs. Parity-converted Cooper pairs should belong to an odd-ω symmetry class to satisfy the Fermi-Dirac statistics (i.e., Berezinskii rule [3]). For example, in a vortex core in a BCS-type SC, odd-ω pairs are induced because of the vortex singularity [23,24]. At the surface of a spin-triplet p-wave SC, odd-ω pairs appear [14,25,26], where surface

Andreev bound states [27] (ABSs) strongly suppress the local pair potential.

Odd-ω pairs in a vortex core are generated by a singularity in real space, whereas odd-ω pairs at the surface generate ABSs, which are related to anisotropy in the momentum space. The two types of odd-ω pairs were considered separately [28]. However, these odd-ω pairs can emerge at the same location and interact with each other. Recently, k_z-dependent anisotropic pairings in three-dimensional (3D) SCs have become realistic (e.g., heavy-fermion compounds [29] and Sr_2RuO_4 [30–33]). In these systems, a quantum vortex can penetrate a two-dimensional (2D) surface hosting flat-band ABSs [34–37]. It is unclear how odd-ω pairs by ABSs affect the odd-ω pairs carrying the vortex supercurrent, and vice versa. Such novel vortex states help determine the pairing symmetry of an SC and can be easily examined by existing experimental methods such as scanning tunneling microscopy [38] (STM) and superconducting quantum interference devices [39,40] (SQUID).

In this study, the interference between odd-ω pairs with two different origins is investigated: the quantum vortex and surface ABSs. A quantum flux penetrating a semi-infinite 3D unconventional SC is considered, where the magnetic flux is perpendicular to the surface, at $z = 0$. Using the quasiclassical Eilenberger theory, the vortex supercurrents and local density of states (LDOS) in the s- and p_z-wave SCs are compared, where surface ABSs are, respectively, absent and present.

The numerical results show that the vortex supercurrent was reversed near the surface where the surface ABSs convert both of the even- and odd-ω pairs into odd- and even-ω ones. The pair amplitude is analyzed and it is shown that there is local symmetry conversion among the Cooper pairs in the region where the vortex and the ABSs coexist. The LDOS, specifically, how the Caroli-de Gennes-Matricon (CdGM) state [38,41,42] and surface ABSs develop when they overlap is investigated. It is also shown that the zero-energy peak in the LDOS split because of the interference.
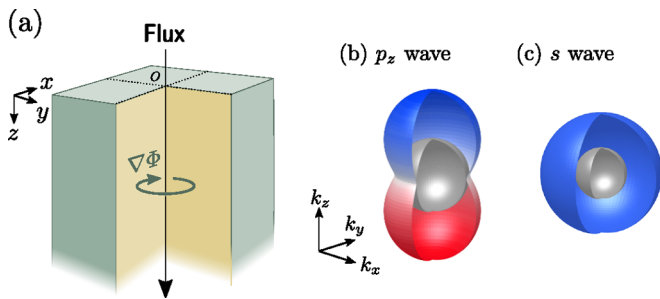
*Corresponding author: s.suzuki-1@utwente.nl

(a)

FIG. 1. (a) Schematic of the system. The vortex core is located where $x = y = 0$ and the semi-infinite 3D SC that occupies $z \geq 0$. The gap amplitudes for the (b) s- and (c) p_z-wave SC, where color means the internal phase of the pair potential. The inner silver sphere indicates the Fermi sphere.

In the analytical calculations, the knowledge gained from the numerical results is extended to more general SCs. By using the Kramer-Pesch approximation [43–45], which is valid at a low temperature and near the vortex core, the direction of the vortex supercurrent near the surface is shown to be determined only by the k_z dependence of the pair potential.

The remainder of this paper is organized as follows. The model and method are introduced in Sec. II. The numerical and analytical results are presented in Secs. III and IV. In Sec. V, the study is summarized.

II. SYSTEM AND FORMULATION

We considered the quantum vortex penetrating a 3D SC as shown in Fig. 1(a). The SC occupies $z \geq 0$ and the vortex core is located at $x = y = 0$. We assume the cylindrical symmetry around the core. We employ the cylindrical coordinate $(x, y, z) = (\rho \cos \Phi, \rho \sin \Phi, z)$.

The superconductivity in the ballistic limit can be described by quasiclassical Eilenberger theory [46–50]. The quasiclassical Green's function obeys the Eilenberger equation,

$$\hbar \boldsymbol{v}_F \cdot \nabla \hat{g} + [\hat{H}, \hat{g}] = 0, \quad \hat{g}^2 = \hat{1},$$

$$\hat{g} = \begin{pmatrix} g & -s_\mu f \\ -\underset{\sim}{f} & -\underset{\sim}{g} \end{pmatrix}, \quad s_\mu = \begin{cases} +1 & \text{for } s \text{ wave,} \\ -1 & \text{for } p_z \text{ wave,} \end{cases} \quad (1)$$

$$\hat{H} = \begin{pmatrix} \omega_n - i(e/c)\boldsymbol{v}_F \cdot \boldsymbol{A} & -s_\mu \Delta \\ -\underset{\sim}{\Delta} & -\omega_n + i(e/c)\boldsymbol{v}_F \cdot \boldsymbol{A} \end{pmatrix},$$

where $\boldsymbol{v}_F = v_F \hat{\boldsymbol{k}}$ with $\hat{\boldsymbol{k}} = (k_x, k_y, k_z) = (\sin \theta \cos \phi, \sin \theta \sin \phi, \cos \theta)$, $\omega_n = (2n + 1)\pi k_B T$, k_B, T, $e < 0$, c, and $\boldsymbol{A}$ are the isotropic Fermi velocity, Matsubara frequency, Boltzmann constant, charge of a quasiparticle, speed of light, and vector potential. The normal and anomalous Green's functions [$g(\hat{\boldsymbol{k}}, \boldsymbol{r}, i\omega_n)$ and $f(\hat{\boldsymbol{k}}, \boldsymbol{r}, i\omega_n)$] describe the quasiparticle and the Cooper pairs. The under-tilde functions have been introduced as $\underset{\sim}{X}(\hat{\boldsymbol{k}}, \boldsymbol{r}, i\omega_n) = X^*(-\hat{\boldsymbol{k}}, \boldsymbol{r}, i\omega_n)$ with X being an arbitral function. In this paper, we refer to f as the pair amplitude. In Eq. (1), we have reduced the spin degree of freedom by assuming the opposite-spin Cooper pairing for both SCs.

We consider the spin-singlet s-wave and spin-triplet p_z-wave SCs whose pair potentials can be given by

$$\Delta(\boldsymbol{r}, \hat{\boldsymbol{k}}) = \begin{cases} \Delta(\boldsymbol{r}) & \text{for } s \text{ wave,} \\ \Delta(\boldsymbol{r})k_z & \text{for } p_z \text{ wave.} \end{cases} \quad (2)$$

The schematic gap functions are shown in Fig. 1. The pair potential $\Delta(\boldsymbol{r})$ is self-consistently determined by the gap equation

$$\Delta(\hat{\boldsymbol{k}}, \boldsymbol{r}) = 2\lambda N_0 \pi k_B T \sum_{n=0}^{N_c} \int \frac{d\Omega'}{4\pi} V(\hat{\boldsymbol{k}}, \hat{\boldsymbol{k}}')f(\boldsymbol{k}', \boldsymbol{r}, i\omega_n),$$

$$\lambda = N_0^{-1} \left(\sum_{n=0}^{N_c} \frac{1}{n + 1/2} + \ln \frac{T}{T_c} \right)^{-1}, \quad (3)$$

where $\int \cdots d\Omega/4\pi$ is the average on the Fermi sphere, N_0 is a density of states (DOS) at Fermi energy in the normal state, and N_c is defined as the positive integer satisfying $N_c < \Omega_c/2\pi k_B T$ with Ω_c being the cut-off frequency. The attractive potential V depends on the pairing symmetry $V = 1$ for the s-wave SC and $V = 3k_z k_z'$ for the p_z wave SC. The pair potential winds its phase around the vortex; $\Delta(\boldsymbol{r}) = \Delta(z, \rho)e^{-i\Phi}$ with $(x, y, z) = (\rho \cos \Phi, \rho \sin \Phi, z)$.

The current density $\boldsymbol{j}(\boldsymbol{r})$ and LDOS $N(\boldsymbol{r}, E)$ are given by

$$\boldsymbol{j}(\boldsymbol{r}) = -4|e|N_0\pi k_B T \sum_{n=0}^{N_c} \int \frac{d\Omega}{4\pi} \boldsymbol{v}_F \text{Im}g(\hat{\boldsymbol{k}}, \boldsymbol{r}, i\omega_n), \quad (4)$$

$$\frac{N(\boldsymbol{r}, E)}{N_0} = \lim_{\delta \to +0} \int \frac{d\Omega}{4\pi} \text{Re}[g(\hat{\boldsymbol{k}}, \boldsymbol{r}, E + i\delta)], \quad (5)$$

where E and δ are the energy and smearing factor. We need to solve the Eilenberger equation and Maxwell equation simultaneously and self-consistently to obtain the magnetic-field distribution [51]. The magnetic field satisfies the following equations [52]:

$$\nabla \times \boldsymbol{A} = \boldsymbol{B}, \quad \nabla \times \boldsymbol{B} = \frac{4\pi}{c}\boldsymbol{j}. \quad (6)$$

In the quasiclassical theory, the Ginzburg-Landau (GL) parameter $\kappa = \lambda_L/\xi$ is a parameter that characterizes the length scale of the magnetic field, where $\lambda_L = \sqrt{3c^2/8\pi e^2 v_F^2 N_0}$ and $\xi = \hbar v_F/2\pi k_B T_c$ are the London penetration depth and coherence length (see the Appendix A for the detail). In the numerical calculations, we set $\kappa = 6\sqrt{6}$ and $\Omega_c = 40k_B T_c$.

III. NUMERICAL RESULTS

A. Paramagnetic quantum vortex

The vector plot of the current density around the vortex core in the p_z-wave SC is shown in Fig. 2(a), where the result for the s-wave SC is shown in Fig. 2(b) as a reference. The color of the vectors corresponds to j_Φ: the red and blue mean the diamagnetic and paramagnetic current respectively. At the surface of the p_z-wave SC, the current density changes its direction near the surface as shown in Fig. 2(a), whereas $\boldsymbol{j}$ in the s-wave case hardly depends on z as shown in Fig. 2(b). The vortex supercurrent inversion can be seen more clearly in the top views in Fig. 2(c). The ρ dependence of j_Φ for the p_z-wave SC is shown in Fig. 3(a), where we fixed the depth at
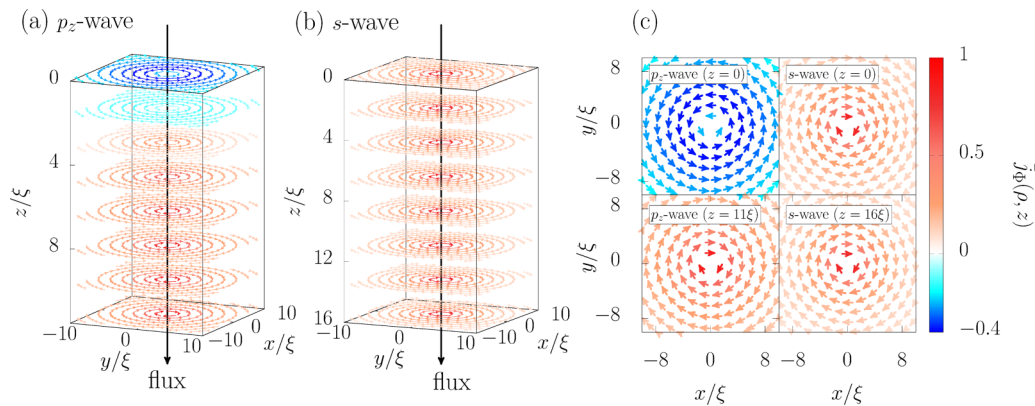
FIG. 2. Vector plots of the current densities at $T/T_c = 0.2$ for (a) the p_z-wave and (b) s-wave SCs. The direction and color of the arrows mean the direction and azimuthal component of the current density. The current density is normalized as $\bar{j}_\Phi = j_\Phi/j_\Phi^{Max}(T/T_c = 0.2)$ with $j_\Phi^{Max}(T/T_c = 0.2)$ being the maximum value of j_Φ at $T/T_c = 0.2$ in each case. The solid black arrows represent the magnetic flux. (c) Top view of the same results at $z = 0$ and $z \gg \xi$. The parameters are set to $\Omega_c = 40k_BT_c$ and $\kappa_{GL} = 6\sqrt{6}$.

$z/\xi = 0, 1, 2, 4, 10$. We see that the profile of j_Φ at $z = 10\xi$ is qualitatively the same as the well-known s-wave result [42]. However, with approaching to the surface, j_Φ changes the sign at $z \sim 2\xi$, meaning that the paramagnetic current flows only near the surface. The self-consistent pair potentials are shown in the Appendix B.

The z component of the local magnetic field B_z for the p_z-wave SC is shown in Fig. 3(b). Deep inside the SC, B_z has the typical profile: the magnetic field has a peak at the vortex core and decays in the order of λ_L. However, with approaching to the surface, B_z is strongly suppressed and spreads broader. Although the paramagnetic current flows near the surface, it does not change sgn[B_z] but modifies significantly the spatial profile of B_z at the surface. We show that the width of the peak in B_z strongly depends on z as in the inset of Fig. 3, where the peak width W_B is defined by using the half-value radius;
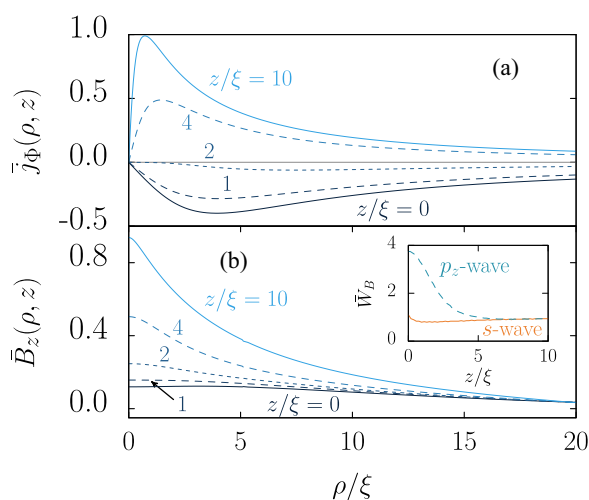
$B_z|_{\rho=W_B} = (1/2)B_z|_{\rho=0}$. In the s-wave case, the peak width does not strongly depends on z. On the contrary, it depends significantly on z in the p_z-wave case. At the surface, W_B is about four times larger than its value at $z = 10\xi$.

The temperature dependence of j_Φ is shown in Fig. 4(a), where j_Φ is obtained at the surface of the p_z-wave SC. The amplitude of the paramagnetic current increases with decreasing temperature. In particular, the paramagnetic current increases rapidly at low temperature. This low-temperature
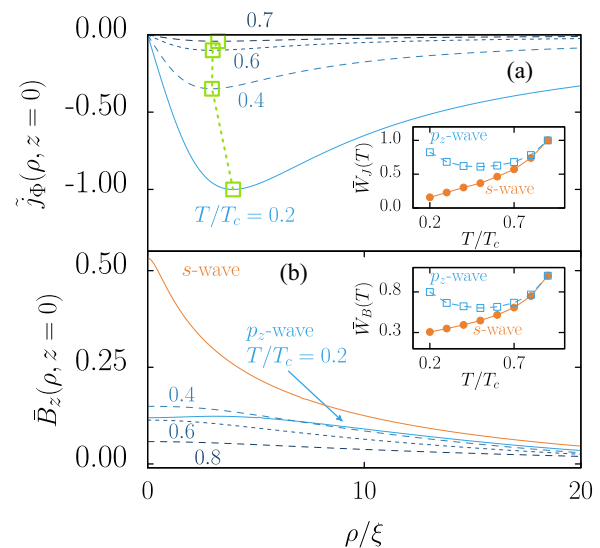

FIG. 3. Spatial profiles of (a) the circulation current and (b) the magnetic field in the p_z-wave SC. The magnetic field is normalized as $\bar{B}_z = B_z/B_z(\rho = 0, z = 10\xi, T/T_c = 0.2)$. The depth is set to $z/\xi = 0, 1, 2, 4,$ and 10. Near the surface, the current changes the direction and the magnetic field is significantly suppressed. The depth dependence of $\bar{W}_B$ is shown in the inset.

FIG. 4. (a) Paramagnetic vortex-current at the surface of the p_z-wave SC. The current density is normalized as $\tilde{j} = j_\Phi/|j_\Phi^{Min}(T/T_c = 0.2)|$ with $j_\Phi^{Min}(T/T_c = 0.2)$ being the minimum value of j_Φ at $T/T_c = 0.2$. The temperature is set to $T/T_c = 0.2, 0.4, 0.6,$ and 0.7. The open squares indicate the maximum value of $|j_\Phi(\rho, z = 0)|$ at each temperature. (b) Magnetic field at the surface of the p_z- and s-wave SCs. The temperature in the p_z-wave SC is set to $T/T_c = 0.2, 0.4, 0.6,$ and 0.8, and the temperature in the s-wave SC is $T/T_c = 0.2$. Insets in (a) and (b) show the temperature dependencies of W_J and W_B, where W_J is defined as $|j_\Phi(\rho = W_J, z = 0, T)| = \max_\rho |j_\Phi(\rho, z = 0, T)|$. We normalize $W_{J(B)}$ as $\bar{W}_{J(B)}(T/T_c = 0.8) = W_{J(B)}/W_{J(B)}(T/T_c = 0.8)$ in each SC.
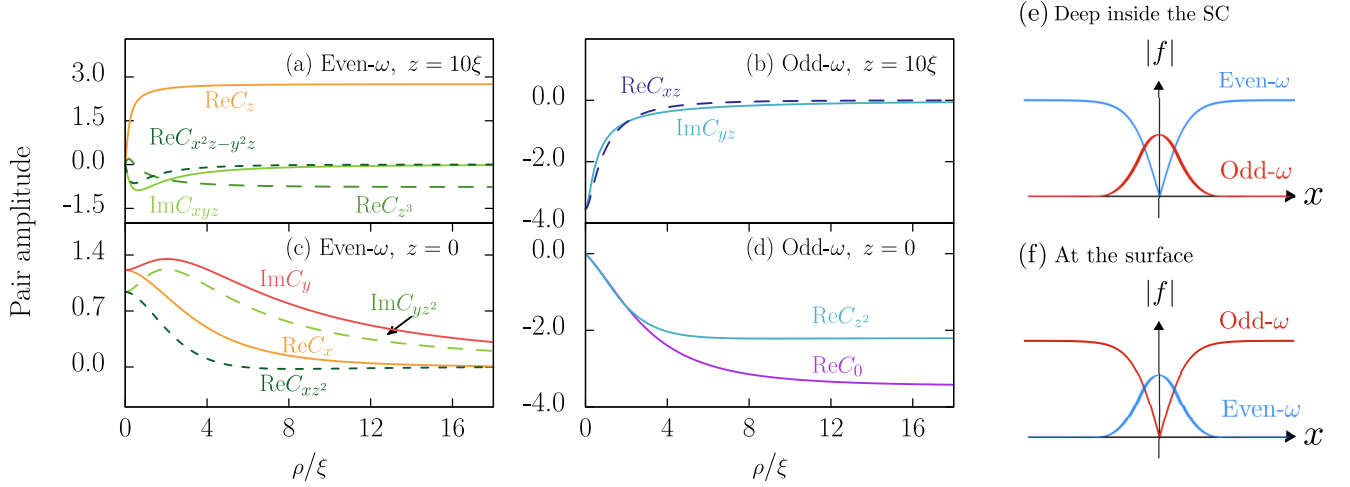
FIG. 5. Pair amplitudes at [(a),(b)] $z = 10\xi$ and [(c),(d)] $z = 0$. The left (right) figures show the even frequency (odd parity) components. The parameters are set to $T = 0.2T_c$, $\omega_n = \omega_0$, and $\Phi = 0$. The definition and notation of $C_{lm}(\boldsymbol{r})$ are shown in Eq. (7) and the Appendix C. The even- and odd-frequency components are subdominant at $z = 0$ and $z = 10\xi$ respectively. The other components are negligibly small. [(e),(f)] Schematic picture of the spatial distribution of the pair amplitudes around the vortex in the p_z-wave SC.

anomaly is characteristic to the paramagnetic response related to the odd-ω pairs induced by the ABSs [6,8–11].

B. Symmetry conversion

We explore the origin of the paramagnetic circulating current in this subsection. The magnetic response is related to the frequency symmetry of Cooper pairs [6–12]. Namely, the direction of the vortex current is determined by the spatial distribution of the even- and odd-ω Cooper pairs. To analyze the symmetry of the Cooper pairs, we expand the pair amplitudes at ω_0 in terms of the real spherical harmonics (see Appendix C for the details),

$$f(\boldsymbol{r}, \boldsymbol{k}, i\omega_0) = \sum_{lm} f_{lm}(\boldsymbol{r}, \boldsymbol{k}), \qquad f_{lm} = C_{lm}(\boldsymbol{r})Y_{lm}(\boldsymbol{k}). \quad (7)$$

We refer to, for example, $f_{l=2,m=2}$ ($d_{x^2-y^2}$-wave component) as $f_{x^2-y^2}$ for simplicity. We hereafter fix $\Phi = 0$ because of the rotational symmetry around the vortex.

Deep inside the p_z-wave SC, the symmetry conversion is caused only by the vortex singularity at $\rho = 0$. In the homogeneous limit, the pair amplitude has only the p_z-wave component, $f = \Delta_\infty k_z/\sqrt{\omega_n^2 + \Delta_\infty k_z^2} \sim f_z + f_{z^3}$ with Δ_∞ being the pair potential in the homogeneous limit, where the denominator induces non-p_z-wave component. At the vortex core, the pair amplitude obtains an additional phase from the phase winding of the vortex, $f \sim k_z(k_x + ik_y) \sim f_{zx} + if_{yz}$ [23,24]. In a spin-triplet SC, these even-parity components should be an odd function of ω_n to satisfy the Pauli exclusion principal (i.e., Berezinskii rule [3]). Figures 5(a) and 5(b) show the symmetry conversion between the even- and odd-ω components at $z = 10\xi$. The even-ω p_z-wave component is dominant at $\rho \gg \xi$, whereas only the odd-ω $d_{zx} + id_{yz}$-wave component has an amplitude at $\rho = 0$.

At the surface, the symmetry conversion is caused by the two factors: the surface ABSs and vortex. The pairing symmetry is shown in Figs. 5(c) and 5(d). At $\rho \gg \xi$, the pair amplitude can be written as a superposition of the s-wave and

d-wave pairings [10,11,25]: $f \sim f_0 + f_{z^2}$. Namely, only the odd-ω pairs are present at the surface far from a vortex. At the intersection of the vortex core and surface (i.e., $\rho = z = 0$), these odd-ω pairs have an additional phase from the vortex. As a result, the $p_x + ip_y$ wave and $f_{xz^2} + if_{yz^2}$ are dominant as shown in Fig. 5(c). Note that these even-ω pairs are generated from the odd-ω pairs, and have different pairing symmetry from the pair potential. In Figs. 5(e) and 5(f), we show the schematics of the spatial profile of the Cooper pairs.

The relation between the frequency-symmetry conversion and supercurrent inversion can be confirmed by analyzing the current density $\boldsymbol{j}$ in Eq. (4). Close to the vortex core (i.e., $\rho \ll \xi$), $\boldsymbol{j}$ can be expressed in terms of the pair amplitudes [10,17,18,53]. Specifically, it can be expressed by the even-ω (odd-ω) component $f_{e(o)}$,

$$j_\Phi(\boldsymbol{r}) = -j_0 \frac{T}{T_c} \sum_{n=0}^{N_c} \int \frac{d\Omega}{4\pi} \sin\theta \sin\phi \, \mathrm{Im} g(\hat{\boldsymbol{k}}, \boldsymbol{r}, i\omega_n), \quad (8)$$

$$g = \sqrt{1 - |f_e|^2 + |f_o|^2 - 2i\,\mathrm{Im} f_o f_e^*}, \quad (9)$$

$$f_{e(o)} = \frac{1}{2}[f(\boldsymbol{r}, \boldsymbol{k}, i\omega_n) + (-)f(\boldsymbol{r}, \boldsymbol{k}, -i\omega_n)], \quad (10)$$

where we have used the normalization condition (i.e., $g^2 = 1 - s_\mu ff$) and $j_0 = 4\pi N_0|e|v_F T_c$. Applying the conversion $f_e \leftrightarrow \tilde{f}_o$ to Eqs. (8) and (9), we show that the frequency-symmetry conversion by the surface ABSs results in the vortex-current inversion (see the Appendix D for the details).

C. Local density of states

Before discussing the obtained quasiparticle spectra, we quickly overview the in-gap states related to this system: Surface ABS and CdGM mode. The p_z-wave SC hosts the surface ABSs [27] at its surface perpendicular to the z direction because of the quasiparticle interference [54]. In the p_z-wave case, the ABSs form the flat-band zero-energy surface states
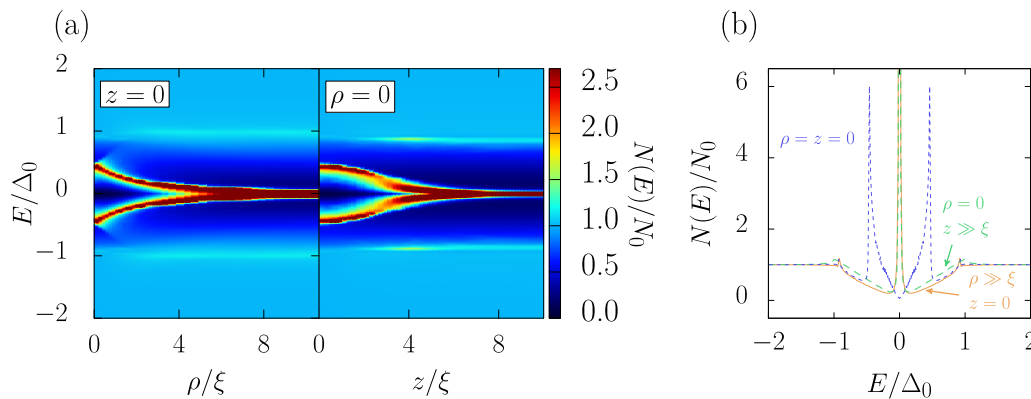
FIG. 6. (a) Contour plots of the LDOS at the surface and the vortex core. (b) Comparison of LDOS. The parameters are set to the same values used in Fig. 2. The smearing factor is $\delta = 0.005$.

[55–57]. The CdGM modes are quasiparticle states bounded at a vortex core [41]. Because of the confinement by the local suppression in the pair potential, the in-gap quasiparticle states appears at the vortex core [58]. In the Appendix B, we show the quasiparticle spectra of the s-wave SC with a vortex as a reference, where we explain the spatial distribution of the CdGM modes.

The LDOS at the surface of the p_z-wave SC are shown in Fig. 6, which can be measured by, for example, a scanning tunnel spectroscopy measurement. The flat-band zero-energy ABSs appear at far from the vortex core (i.e., $\rho \gg \xi$). Approaching to the vortex, the bound-states energy is lifted from $E = 0$ and the zero-energy peak is split into two peaks with $E \approx 0.5\Delta_\infty$ at $\rho = 0$. The evolution of the CdGM modes at the lowest energy are shown in Fig. 6, where we fix $\rho = 0$. Deep inside the SC ($z \gg \xi$), the CdGM mode stay at $E \approx 0$. However, with approaching to the surface, the zero-energy peak splits into two peaks. We conclude the zero-energy peak splitting is a result of the interference between the surface ABSs from the p_z-wave nature and the CdGM modes from the quantum vortex: The quantum states staying at $E = 0$ repel each other in energy space due to the superposition in real space.

The splitting of the LDOS at $E = 0$ can also be interpreted in another way. The ABS appears at the zero-energy when $\Delta(\mathbf{k}_{\text{in}}) = -\Delta(\mathbf{k}_{\text{out}})$ during the reflection at a surface, where $\mathbf{k}_{\text{in}}$ ($\mathbf{k}_{\text{out}}$) is the incoming (outgoing) momentum. A similar

sign change occurs when the quasiparticle passes through the vortex core. However, on the quasiclassical paths passing through the origin (intersection of the surface and the vortex core), this sign change never occurs. The sign change from the reflection and that from the vortex core compensate each other. Therefore, the zero-energy state does not appear at the origin.

IV. KRAMER-PESCH THEORY

We apply the Kramer-Pesch approximation [43–45] to more general superconducting states and generalize our results obtained numerically; the vortex-current reversal and disappearance of the zero-energy peak at $z = \rho = 0$ in the LDOS. The Kramer-Pesch approximation, which is valid when $k_B T \ll |\Delta_\infty|$ and $\rho \ll \xi$, allow us to obtain the analytic solution of the quasiclassical Green's function. We assume that the gap function is written as

$$\Delta(\mathbf{r}, \hat{\mathbf{k}}) = h(\rho, z) e^{-i\Phi} \Psi(\hat{\mathbf{k}}), \tag{11}$$

where $h(\rho, z)$ is a real function describing the spatial profile of Δ and $\Psi(\hat{\mathbf{k}})$ is the momentum dependence of Δ, which satisfies $\Psi(\mathbf{k}_\parallel, k_z) = s_\theta \Psi(\mathbf{k}_\parallel, -k_z)$ with $\mathbf{k}_\parallel = (k_x, k_y, 0)$ and $s_\theta = \pm 1$. Surface ABSs are formed when $s_\theta = -1$. In the Kramer-Pesch approximation, the azimuthal components of current density j_Φ for each s_θ are written as

$$j_\Phi(\mathbf{r})|_{s_\theta=1} \simeq 4\pi N_0 |e| v_F \int \frac{d\Omega}{4\pi} \sin^2(\phi - \Phi) \frac{C^{-1}}{4k_B T} \rho \tilde{D}, \tag{12}$$

$$j_\Phi(\mathbf{r})|_{s_\theta=-1} \leqslant 4\pi N_0 |e| v_F \int \frac{d\Omega}{4\pi} \sin^2(\phi - \Phi) \left[-\frac{C^{-1}}{8k_B T} + \frac{2}{C^{-1}} \right] \rho \tilde{D}, \tag{13}$$

$$\tilde{D}(\rho, \Phi, \mathbf{k}) = \frac{2}{v_F C(\rho, \Phi, \mathbf{k})} \int_{-\infty}^{\infty} d\sigma' \frac{1}{\sigma'} h\left(|\sigma| \sin\theta, \left| \sigma \cos\theta - \rho \frac{\cos(\phi - \Phi)}{\tan\theta} \right| \right) \exp\left[-2|\Psi(\mathbf{k})| \bar{F}(\rho, \Phi, \sigma', \mathbf{k}) \right], \tag{14}$$

$$C(\rho, \Phi, \mathbf{k}) = \frac{2}{v_F} \int_{-\infty}^{\infty} d\sigma' \exp\left[-2|\Psi(\mathbf{k})| \bar{F}(\rho, \Phi, \sigma', \mathbf{k}) \right], \tag{15}$$

$$\bar{F}(\rho, \Phi, \sigma, \hat{\mathbf{k}}) = \int_{\rho \cos(\phi - \Phi)(\sin\theta)^{-1}}^{\sigma} \text{sign}(\sigma') h(|\sigma'| \sin\theta, |\sigma' \cos\theta + z_0|) d\sigma', \tag{16}$$

where $\tilde{D} \geqslant 0$ and $C \geqslant 0$. The detailed derivation of Eq. (13) is explained in the Appendix E. The conventional vortex current has a positive value as in Eq. (12). On the other hand, Eq. (13) shows that the current density can be negative at low temperature because of the first term. Thus, the vortex current on the surface with the ABS is reversed.

In the Kramer-Pesch approximation, the surface DOS for $s_\theta = -1$ is written as

$$\frac{N(E, \rho, z=0)}{N_0} = \int \frac{d\Omega}{4\pi} \frac{(\rho D + E)^2}{(\rho D + E)^2 + C^{-2}} \leqslant 1, \quad (17)$$

$$D = \frac{\sin(\phi - \Phi)}{\sin \theta} \tilde{D}. \quad (18)$$

Equation (17) shows that the surface DOS is less than N_0 and becomes zero at $\rho = E = 0$ (see the Appendix E for the details.). Therefore, the zero-energy peak in the LDOS at $\rho = z = 0$ disappears when $s_\theta = -1$.

Applying the Kramer-Pesch approximation, we demonstrate the current inversion and the disappearance of the zero-energy peak in the LDOS under the condition $\Delta(k_x, k_y, k_z) = -\Delta(k_x, k_y, -k_z)$. This indicates that our numerical results are not unique only to the p_z-wave SC. The vortex supercurrent inversion can occur in superconductors with flat-band surface ABSs.

V. CONCLUSIONS

We have demonstrated that the local frequency-symmetry conversion of Cooper pairs inverts the direction of the vortex supercurrent. Using the quasiclassical Eilenberger theory, a quantum vortex penetrating a surface hosting the ABSs both numerically and analytically has been investigated. In the self-consistent simulations, comparing the vortex supercurrents in the p_z-wave and s-wave SCs, we have found that the supercurrent flows in the opposite direction near the surface of the p_z-wave SC. By analyzing the anomalous Green's function, the frequency-symmetry conversion among Cooper pairs by ABSs has been shown to trigger the supercurrent inversion. In the analytic calculation with the Kramer-Pesch approximation, the condition of the vortex current inversion has been generalized.

From the quasiparticle spectra obtained from the Green's function, we have found that the zero-energy states from the ABSs and CdGM mode are coupled with each other and shift to nonzero energies when the current inversion occurred. Within the Kramer-Pesch approximation, it has been analytically shown that the LDOS is zero at the intersection of the vortex core and surface because of the interference between the ABSs and CdGM mode.

ACKNOWLEDGMENTS

APPENDIX A: MAXWELL EQUATION, RICCATI PARAMETRIZATION, AND BOUNDARY CONDITIONS

In this section, we introduce the formulations of the vector potential, Riccati parametrization, and boundary conditions. Under the rotational symmetry around the z axis, the magnetic field $\boldsymbol{B}$ and vector potential $\boldsymbol{A}$ are obtained from $\boldsymbol{j}$ as

$$\boldsymbol{B}(\boldsymbol{r}) = \frac{1}{c} \int \boldsymbol{j}(\boldsymbol{r}') \times \frac{\boldsymbol{r} - \boldsymbol{r}'}{|\boldsymbol{r} - \boldsymbol{r}'|^3} dV', \quad (A1)$$

$$\boldsymbol{A}(\boldsymbol{r}) = \boldsymbol{e}_\Theta \int_z^\infty B_\rho(\rho, z')dz' + \boldsymbol{e}_\Theta \frac{1}{\rho} \int_0^\rho \rho' B_z(\rho', z = \infty)d\rho'. \quad (A2)$$

We introduce a dimensionless Maxwell equation (6) for numerical calculations,

$$\nabla' \times (\nabla' \times \boldsymbol{A}') = \frac{6}{\kappa^2} \boldsymbol{j}', \quad (A3)$$

where $\nabla' = \xi \nabla$, $\boldsymbol{A}$ and $\boldsymbol{j}$ are normalized as $\boldsymbol{A}' = (2\pi\xi/\Phi_0)\boldsymbol{A}$ and $\boldsymbol{j}' = \boldsymbol{j}/j_0$ with $\Phi_0 = \pi\hbar c/|e|$ and $j_0 = 4\pi N_0|e|v_F T_c$.

In order to solve the Eilenberger equation (1) numerically, we introduce the coherence function [49,50] γ as

$$g = \frac{1 - s_\mu \gamma \underset{\sim}{\gamma}}{1 + s_\mu \gamma \underset{\sim}{\gamma}}, \quad f = \frac{2\gamma}{1 + s_\mu \gamma \underset{\sim}{\gamma}}. \quad (A4)$$

Substituting Eq. (A4) into Eq. (1), we obtain the Riccati-type differential equations,

$$\hbar \boldsymbol{v}_F \cdot \nabla \gamma - 2\left(\omega_n - \frac{ie}{c} \boldsymbol{v}_F \cdot \boldsymbol{A}\right)\gamma - \Delta + \Delta^* \gamma^2 = 0, \quad (A5)$$

$$\hbar \boldsymbol{v}_F \cdot \nabla \underset{\sim}{\gamma} + 2\left(\omega_n - \frac{ie}{c} \boldsymbol{v}_F \cdot \boldsymbol{A}\right)\underset{\sim}{\gamma} + s_\mu \Delta^* - s_\mu \Delta \underset{\sim}{\gamma}^2 = 0. \quad (A6)$$

The solutions of Eq. (1) are given by solving Eq. (A5) and (A6) along the quasiclassical paths and substituting the obtained γ and $\underset{\sim}{\gamma}$ into Eq. (A4). We solve Eqs. (3), (A2), (A5), and (A6) numerically in a self-consistent manner. The coherence functions γ and $\underset{\sim}{\gamma}$ in the homogeneous limit (i.e., $\nabla \cdot \gamma = 0$) are given by

$$\gamma = \frac{\Delta_\infty}{\omega_n + \text{sign}(\omega_n)\sqrt{\omega_n^2 + |\Delta_\infty|^2}}, \quad (A7)$$

$$\underset{\sim}{\gamma} = \frac{s_\mu \Delta_\infty^*}{\omega_n + \text{sign}(\omega_n)\sqrt{\omega_n^2 + |\Delta_\infty|^2}}, \quad (A8)$$

where Δ_∞ is the bulk value of Δ.

We impose the boundary conditions on the coherence functions. (I) The coherence functions are equal to the values in Eqs. (A7) and (A8) deep inside the SC (i.e., $\rho \gg \xi$, $z \gg \xi$). (II) At the surface (i.e., $z = 0$), we impose

$$\gamma(\hat{\boldsymbol{k}}_\parallel, \hat{k}_z, \boldsymbol{r}_\parallel, z = 0, i\omega_n) = \gamma(\hat{\boldsymbol{k}}_\parallel, -\hat{k}_z, \boldsymbol{r}_\parallel, z = 0, i\omega_n), \quad (A9)$$
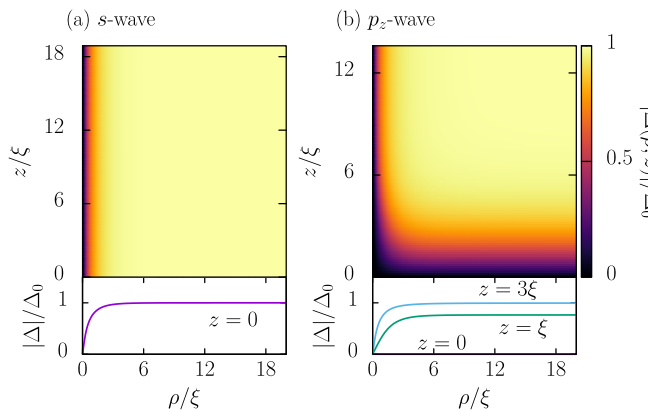
FIG. 7. Spatial dependencies of $|\Delta|$ in the (a) s-wave and (b) p_z-wave SCs. The pair potential is normalized by its bulk value. The parameters are set to $T/T_c = 0.2$, $\Omega_c = 40k_B T_c$, and $\kappa_{GL} = 6\sqrt{6}$.
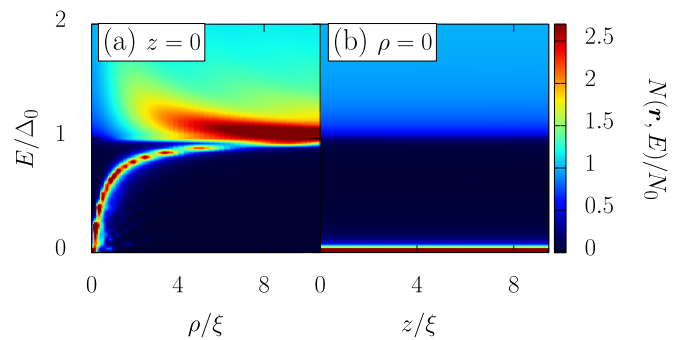

FIG. 8. Contour plots of the LDOS at (a) surface and (b) vortex core in the s-wave SC. The parameters are the same as in Fig. 7. The smearing factor is $\delta = 0.005$.

which means the specular reflection where $\boldsymbol{r}_\parallel = (x, y)$. As a result of Eq. (A9), the pair amplitude f is forced to be an even function with respects to the k_z inversion at the surface.

APPENDIX B: ADDITIONAL NUMERICAL RESULTS

In this section, we show the spatial dependence of the pair potential and local density of state (LDOS) for the s-wave SC. We show the spatial dependencies of the pair potential in Fig. 7. As shown in Fig. 7(a), the pair potential in the s-wave SC is suppressed near the vortex core but not at the surface. On the other hand, the pair function in the p_z-wave SC disappears at the vortex core and the surface as shown in Fig. 7(b).

In Fig. 8, we show the LDOS in the s-wave SC. Figures 8(a) and 8(b) show the LDOS at the surface and vortex core. In Fig. 8, there exist subgap bound states near the core known as the Caroli-de-Gennes-Matricon (CdGM) modes. The approximate energy dispersion of the CdGM modes have been derived as $E_n \simeq (n - 1/2)\Delta_\infty^2 / E_F$ in Ref. [41], where the half integer $(n - 1/2)$ is the quantum number of the angular momentum. The eigenfunction of the CdGM mode labeled by n has a maximum amplitude at a radius distance of the order $\rho \simeq (n - 1/2)/k_F$ [42]. Thus, the evolution of subgap states in Fig. 8(a) corresponds to the dispersion relation of the CdGM modes.

TABLE I. Notation of the expansion coefficients f_{lm}.

l	m	Orbital	Real spherical harmonics Y_{lm}	Notation of f_{lm}
0	0	s	$\sqrt{(1/4\pi)}$	f_0
1	-1	p_y	$\sqrt{(3/4\pi)}\sin\phi\sin\theta$	f_y
	0	p_z	$\sqrt{(3/4\pi)}\cos\theta$	f_z
	1	p_x	$\sqrt{(3/4\pi)}\cos\phi\sin\theta$	f_x
2	-2	d_{xy}	$\sqrt{(15/16\pi)}\sin 2\phi\sin^2\theta$	f_{xy}
	-1	d_{yz}	$\sqrt{(15/16\pi)}\sin\phi\sin 2\theta$	f_{yz}
	0	d_{z^2}	$\sqrt{(5/16\pi)}\left(3\cos^2\theta - 1\right)$	f_{z^2}
	1	d_{xz}	$\sqrt{(15/16\pi)}\cos\phi\sin 2\theta$	f_{xz}
	2	$d_{x^2-y^2}$	$\sqrt{(15/16\pi)}\cos 2\phi\sin^2\theta$	$f_{x^2-y^2}$
3	-3	$f_{y(3x^2-y^2)}$	$\sqrt{(35/32\pi)}\sin 3\phi\sin^3\theta$	$f_{y(3x^2-y^2)}$
	-2	f_{xyz}	$\sqrt{(105/16\pi)}\sin 2\phi\sin^2\theta\cos\theta$	f_{xyz}
	-1	f_{yz^2}	$\sqrt{(21/32\pi)}\sin\phi\sin\theta\left(5\cos^2 -1\right)$	f_{yz^2}
	0	f_{z^3}	$\sqrt{(7/16\pi)}\left(5\cos^3\theta - 3\cos\theta\right)$	f_{z^3}
	1	f_{xz^2}	$\sqrt{(21/32\pi)}\cos\phi\sin\theta\left(5\cos^2 -1\right)$	f_{xz^2}
	2	$f_{z(x^2-y^2)}$	$\sqrt{(105/16\pi)}\cos 2\phi\sin^2\theta\cos\theta$	$f_{z(x^2-y^2)}$
	3	$f_{x(x^2-3y^2)}$	$\sqrt{(35/32\pi)}\cos 3\phi\sin^3\theta$	$f_{x(x^2-3y^2)}$

APPENDIX C: RENORMALIZED SPHERICAL HARMONICS

We use the real spherical harmonics Y_{lm} to analyze the pair amplitudes. We abbreviate the expansion coefficients f_{lm} in the main texts for simplicity. We summarize Y_{lm} and the notation of f_{lm} in Table I. The spherical harmonics Y_{lm} is normalized to satisfy the orthonormal relation

$$\int Y_{lm} Y_{l'm'} d\Omega = \delta_{ll'} \delta_{mm'}, \tag{C1}$$

where $d\Omega = \sin\theta \, d\phi \, d\theta$.

APPENDIX D: VORTEX SUPERCURRENT AND FREQUENCY SYMMETRY OF COOPER PAIRS

The direction of the vortex supercurrent is related to the frequency symmetry of Cooper pairs. The azimuthal component of the current density (4) is

$$j_\Phi(\boldsymbol{r}) = -j_0 \frac{T}{T_c} \sum_{n=0}^{N_c} \int \frac{d\Omega}{4\pi} \sin\theta \sin\phi \, \mathrm{Im} g(\hat{\boldsymbol{k}}, \boldsymbol{r}, i\omega_n), \tag{D1}$$

where $j_0 = 4\pi N_0 |e| v_F T_c$. Namely, the direction of the current is determined by the sign of $\mathrm{Im}[g]$. Using the normalization condition for the quasiclassical Green's function (i.e., $g^2 = 1 - s_\mu f \underset{\sim}{f}$), we have

$$g = \sqrt{1 - |f_e|^2 + |f_o|^2 - 2i \mathrm{Im} f_o f_e^*}, \tag{D2}$$

$$f_{e(o)} = \frac{1}{2}[f(\boldsymbol{r}, \boldsymbol{k}, i\omega_n) + (-)f(\boldsymbol{r}, \boldsymbol{k}, -i\omega_n)], \tag{D3}$$

where f_e and f_o represent respectively the even- and odd-frequency component, and we have used the symmetry relation between f and $\underset{\sim}{f}$ [i.e., $\underset{\sim}{f}(\boldsymbol{r}, \boldsymbol{k}, i\omega_n) = f^*(\boldsymbol{r}, -\boldsymbol{k}, i\omega_n)$].

We analyze the direction of the vortex supercurrent in the vicinity of the vortex core. From Fig. 5(e), deep inside the SC, the pair amplitudes around the vortex core can be approximated as

$$f_e \approx \rho F, \quad f_o \approx -RFe^{-i\phi}, \tag{D4}$$

where $F = F(\hat{\boldsymbol{k}})$ and we have introduced the constant R ($0 < R < 1$) that expresses the relative amplitude of f_o to f_e. The subdominant component has an additional phase factor $(-e^{-i\phi})$ from the phase winding of the vortex. Substituting Eq. (D4) into Eq. (D2), we have

$$g = \sqrt{1 - \rho^2 |F|^2 + R^2 |F|^2 + 2i\rho R |F|^2 \mathrm{Im} e^{-i\phi}} \tag{D5}$$

$$= \sqrt{1 + R^2 |F|^2} - i\rho \frac{R|F|^2 \sin\phi}{\sqrt{1 + R^2 |F|^2}} + O(\rho^2) \tag{D6}$$

with $\rho \ll \xi$. The equation above results in

$$-j_0 \sin\phi \mathrm{Im} g = \rho \frac{j_0 R |F|^2 \sin^2\phi}{\sqrt{1 + R^2 |F|^2}} + O(\rho^2), \tag{D7}$$

meaning that the electric current flows in the opposite direction of the phase winding $e^{-i\Phi}$ around the vortex core (i.e., $j_\Phi > 0$).

At the surface of a p_z-wave SC, the symmetry conversion occurs because of the ABSs. From Fig. 5(f), the pair ampli-

tudes can be expressed as

$$f_e = -RFe^{-i\phi}, \quad f_o = \rho F, \tag{D8}$$

where we can show $R^2 |F|^2 = 1$ by solving the Riccati-type differential equations (E1) at $T = 0$ and $\rho = 0$. We assume f_e near the core has the maximum value at $\omega_n = 0$. From this assumption, we obtain $R^2 |F|^2 < 1$ at finite Matsubara frequencies. Substituting Eq. (D8) into Eq. (D2), we have

$$g = \sqrt{1 - R^2 |F|^2 + \rho^2 |F|^2 + 2i\rho R |F|^2 \mathrm{Im} e^{i\phi}} \tag{D9}$$

$$= \sqrt{1 - R^2 |F|^2} + i\rho \frac{R|F|^2 \sin\phi}{\sqrt{1 - R^2 |F|^2}} + O(\rho^2). \tag{D10}$$

Therefore, the direction of the current density is given by

$$-j_0 \sin\phi \mathrm{Im}[g] = -\rho \frac{j_0 R |F|^2 \sin^2\phi}{\sqrt{1 - R^2 |F|^2}} + O(\rho^2). \tag{D11}$$

Comparing Eqs. (D7) and (D11), we see that the frequency-symmetry conversion results in the vortex-current inversion.

APPENDIX E: ANALYTICAL CALCULATIONS BY KRAMER-PESCH APPROXIMATION

In this section, we analytically calculate the quasiclassical Green's functions by the Kramer-Pesch approximation [43–45] and reproduce two numerical results, the reversal of the vortex current and suppression of the LDOS at the intersection point of the surface and vortex core, for more general SCs. In the Kramer-Pesch approximation, we obtain the solutions of the Riccati-type differential equations up to the first order of the displacement b from the vortex core and Matsubara frequency ω_n. Thus, the Kramer-Pesch approximation is appropriate near the vortex core $\rho \ll \xi$ and in low temperature $k_B T \ll |\Delta|$. In this section, We follow the method in Ref. [44].

We start with the Riccati-type differential equations with $\boldsymbol{A} = 0$,

$$\boldsymbol{v}_F \cdot \boldsymbol{\nabla}\gamma + 2\omega_n\gamma - \Delta + \Delta^*\gamma^2 = 0, \tag{E1}$$

$$\boldsymbol{v}_F \cdot \boldsymbol{\nabla}\underset{\sim}{\gamma} - 2\omega_n\underset{\sim}{\gamma} + s_\mu\Delta^* - s_\mu\Delta\underset{\sim}{\gamma}^2 = 0, \tag{E2}$$

where we use the units $\hbar = k_B = 1$. We introduce the coordinate transformation as in Fig. 9,

$$a = x\cos\phi + y\sin\phi, \tag{E3}$$

$$b = -x\sin\phi + y\cos\phi, \tag{E4}$$

where the angle ϕ characterizes the direction of the momentum $\hat{\boldsymbol{k}} = (\sin\theta\cos\phi, \sin\theta\sin\phi, \cos\theta)$. The b axis is perpendicular to the projected momentum $\boldsymbol{k}_\parallel = (\sin\theta\cos\phi, \sin\theta\sin\phi, 0)$. We solve the Riccati-type differential equations by integrating γ or $\underset{\sim}{\gamma}$ in the direction $\hat{\boldsymbol{k}}$. The impact parameter b is constant on the integrating path and corresponds to the distance between the integrating path and vortex core. In this coordinate $\boldsymbol{r} = (a, b, z)$, the Riccati-type
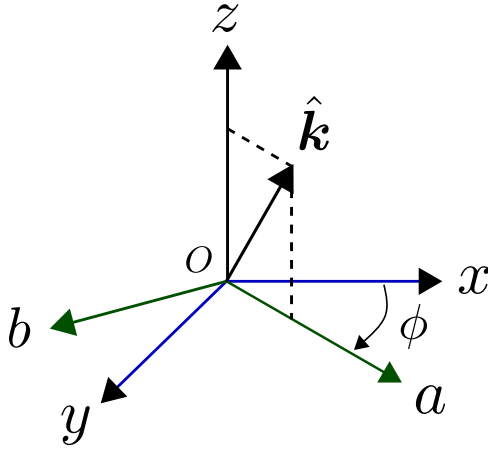
FIG. 9. Coordinate transformation from (x, y, z) to (a, b, z).

differential equations are rewritten as

$$v_F\left\{\sin\theta\frac{\partial}{\partial a} + \cos\theta\frac{\partial}{\partial z}\right\}\gamma + 2\omega_n\gamma - \Delta + \Delta^*\gamma^2 = 0, \quad \text{(E5)}$$

$$v_F\left\{\sin\theta\frac{\partial}{\partial a} + \cos\theta\frac{\partial}{\partial z}\right\}\underset{\sim}{\gamma} - 2\omega_n\underset{\sim}{\gamma} + s_\mu\Delta^* - s_\mu\Delta\underset{\sim}{\gamma}^2 = 0. \quad \text{(E6)}$$

In the analytic calculation, the pair potential is written in more general form

$$\Delta(\hat{\boldsymbol{k}}) = h(\rho, z)e^{-i\Phi}\Psi(\hat{\boldsymbol{k}}), \quad \text{(E7)}$$

where the real function h and the complex function Ψ describe the spatial and momentum dependence of Δ. In addition, we assume that Ψ satisfies $s_\theta = \Psi(\theta, \phi)/\Psi(\pi - \theta, \phi) = \pm 1$. In the case of $s_\theta = 1$ and -1, the ABSs is absence and present on the surface perpendicular to the z axis. We expand the pair potential as

$$\Delta(\hat{\boldsymbol{k}}, \boldsymbol{r}) = \Delta_0 + \Delta_1, \quad \text{(E8)}$$

$$\Delta_0 = h(|a|, z)e^{-i\phi}\text{sign}(a)\Psi(\hat{\boldsymbol{k}}), \quad \text{(E9)}$$

$$\Delta_1 = -h(|a|, z)e^{-i\phi}\text{sign}(a)i\frac{b}{a}\Psi(\hat{\boldsymbol{k}}), \quad \text{(E10)}$$

with respect to b. The solutions (A7) and (A8) in the homogeneous limit are also expanded in terms of b and ω_n as

$$\gamma(\boldsymbol{r}, \hat{\boldsymbol{k}}, i\omega_n) = \text{sign}(a\omega_n)\left\{\frac{\Psi(\hat{\boldsymbol{k}})e^{-i\phi}}{|\Psi(\hat{\boldsymbol{k}})|} - \frac{\Psi(\hat{\boldsymbol{k}})e^{-i\phi}}{h(|a|, z)|\Psi(\hat{\boldsymbol{k}})|^2}|\omega_n| - i\frac{\Psi(\hat{\boldsymbol{k}})e^{-i\phi}}{|\Psi(\hat{\boldsymbol{k}})|}\frac{b}{a}\right\} + \cdots, \quad \text{(E11)}$$

$$\underset{\sim}{\gamma}(\boldsymbol{r}, \hat{\boldsymbol{k}}, i\omega_n) = \text{sign}(a\omega_n)\left\{\frac{s_\mu\Psi^*(\hat{\boldsymbol{k}})e^{i\phi}}{|\Psi(\hat{\boldsymbol{k}})|} - \frac{s_\mu\Psi^*(\hat{\boldsymbol{k}})e^{i\phi}}{h(|a|, z)|\Psi(\hat{\boldsymbol{k}})|^2}|\omega_n| + i\frac{s_\mu\Psi^*(\hat{\boldsymbol{k}})e^{i\phi}}{|\Psi(\hat{\boldsymbol{k}})|}\frac{b}{a}\right\} + \cdots. \quad \text{(E12)}$$

When we set the cut-off of the integral path as $a_c > 0$, the boundary conditions (I) in the Appendix A are given for $\omega_n > 0$ as

$$\gamma\left(a = -a_c, \frac{\pi}{2} < \theta \leqslant \pi, i\omega_n\right) = -\frac{\Psi(\hat{\boldsymbol{k}})e^{-i\phi}}{|\Psi(\hat{\boldsymbol{k}})|} + \frac{\Psi(\hat{\boldsymbol{k}})e^{-i\phi}}{\Delta_0|\Psi(\hat{\boldsymbol{k}})|^2}|\omega_n| - i\frac{\Psi(\hat{\boldsymbol{k}})e^{-i\phi}}{|\Psi(\hat{\boldsymbol{k}})|}\frac{b}{a_c}, \quad \text{(E13)}$$

$$\underset{\sim}{\gamma}\left(a = a_c, 0 \leqslant \theta < \frac{\pi}{2}, i\omega_n\right) = \frac{s_\mu\Psi^*(\hat{\boldsymbol{k}})e^{i\phi}}{|\Psi(\hat{\boldsymbol{k}})|} - \frac{s_\mu\Psi^*(\hat{\boldsymbol{k}})e^{i\phi}}{\Delta_0|\Psi(\hat{\boldsymbol{k}})|^2}|\omega_n| + i\frac{s_\mu\Psi^*(\hat{\boldsymbol{k}})e^{i\phi}}{|\Psi(\hat{\boldsymbol{k}})|}\frac{b}{a_c}, \quad \text{(E14)}$$

The Riccati-type differential equations of the zeroth order of b and ω_n are written as

$$v_F\left\{\sin\theta\frac{\partial}{\partial a} + \cos\theta\frac{\partial}{\partial z}\right\}\gamma_0 - \Delta_0 + \Delta_0^*\gamma_0^2 = 0, \quad \text{(E15)}$$

$$v_F\left\{\sin\theta\frac{\partial}{\partial a} + \cos\theta\frac{\partial}{\partial z}\right\}\underset{\sim}{\gamma}_0 + s_\mu\Delta_0^* - s_\mu\Delta_0\underset{\sim}{\gamma}_0^2 = 0. \quad \text{(E16)}$$

The solutions of these equations for $\omega_n > 0$ are given by

$$\gamma_0(\hat{\boldsymbol{k}}, i\omega_n) = -\frac{\Psi(\max\{\theta, \pi - \theta\}, \phi)}{|\Psi(\hat{\boldsymbol{k}})|}e^{-i\phi}, \quad \text{(E17)}$$

$$\underset{\sim}{\gamma}_0(\hat{\boldsymbol{k}}, i\omega_n) = \frac{s_\mu\Psi^*(\min\{\theta, \pi - \theta\}, \phi)}{|\Psi(\hat{\boldsymbol{k}})|}e^{i\phi}, \quad \text{(E18)}$$

which satisfies the boundary conditions (A9), (E13), and (E14). The first-order Riccati-type differential equations are written as

$$v_F\left\{\sin\theta\frac{\partial}{\partial a} + \cos\theta\frac{\partial}{\partial z}\right\}\gamma_1 + 2\omega_n\gamma_0 - \Delta_1 + 2\Delta_0^*\gamma_0\gamma_1 + \Delta_1^*\gamma_0^2 = 0, \quad \text{(E19)}$$

$$v_F\left\{\sin\theta\frac{\partial}{\partial a} + \cos\theta\frac{\partial}{\partial z}\right\}\underset{\sim}{\gamma}_1 - 2\omega_n\underset{\sim}{\gamma}_0 + s_\mu\Delta_1^* - 2s_\mu\Delta_0\underset{\sim}{\gamma}_0\underset{\sim}{\gamma}_1 - s_\mu\Delta_1\underset{\sim}{\gamma}_0^2 = 0. \quad \text{(E20)}$$

The general solutions of these equations are given as

$$
\gamma_1 = \frac{2}{v_F} \exp[2|\Psi(\hat{\boldsymbol{k}})|F(\sigma, z_0, \theta)] \int_{\sigma_0}^{\sigma} d\sigma' \left[-i\frac{b}{\sigma' \sin\theta} \Delta_0 - \omega_n \gamma_0 \right] \exp[-2|\Psi(\hat{\boldsymbol{k}})|F(\sigma', z_0, \theta)]
$$
$$
+ C_0 \exp[2|\Psi(\hat{\boldsymbol{k}})|F(\sigma, z_0, \theta)], \tag{E21}
$$

$$
\underset{\sim}{\gamma_1} = \frac{2}{v_F} \exp[2s_\theta|\Psi(\hat{\boldsymbol{k}})|F(\sigma, z_0, \theta)] \int_{\underset{\sim}{\sigma_0}}^{\sigma} d\sigma' \left[-is_\mu \frac{b}{\sigma' \sin\theta} \Delta_0^* + \omega_n \underset{\sim}{\gamma_0} \right] \exp[-2s_\theta|\Psi(\hat{\boldsymbol{k}})|F(\sigma', z_0, \theta)]
$$
$$
+ \underset{\sim}{C_0} \exp[2s_\theta|\Psi(\hat{\boldsymbol{k}})|F(\sigma, z_0, \theta)], \tag{E22}
$$

$$
F(\sigma, z_0, \theta) = \int_{-\frac{z_0}{\cos\theta}}^{\sigma} \operatorname{sign}(\sigma') \frac{\Psi(\max\{\theta, \pi - \theta\}, \phi)}{\Psi(\boldsymbol{k})} h(|\sigma'| \sin\theta, \sigma' \cos\theta + z_0) d\sigma', \tag{E23}
$$

$$
a = \sigma \sin\theta, \tag{E24}
$$

$$
z = \sigma \cos\theta + z_0, \tag{E25}
$$

where $\sigma_0, C_0, \underset{\sim}{\sigma_0}$, and $\underset{\sim}{C_0}$ are integral constants. In $\pi/2 < \theta \leqslant \pi$, we obtain the first-order coherence function γ_1 from the boundary condition (E13) as

$$
\gamma_1 = \frac{2}{v_F} \exp[2|\Psi(\hat{\boldsymbol{k}})|F(\sigma, z_0, \theta)] \int_{-\frac{a_c}{\sin\theta}}^{\sigma} d\sigma' \left[-i\frac{b}{\sigma' \sin\theta} \Delta_0 - \omega_n \gamma_0 \right] \exp[-2|\Psi(\hat{\boldsymbol{k}})|F(\sigma', z_0, \theta)]
$$
$$
+ \left\{ \frac{\Psi(\hat{\boldsymbol{k}})e^{-i\phi}}{\Delta_\infty |\Psi(\hat{\boldsymbol{k}})|^2} |\omega_n| - i\frac{\Psi(\hat{\boldsymbol{k}})e^{-i\phi}}{|\Psi(\hat{\boldsymbol{k}})|} \frac{b}{a_c} \right\} \exp\left[2|\Psi(\hat{\boldsymbol{k}})| \left\{ F(\sigma, z_0, \theta) - F\left(-\frac{a_c}{\sin\theta}, z_0, \theta \right) \right\} \right]. \tag{E26}
$$

The other function $\underset{\sim}{\gamma_1}$ in $0 \leqslant \theta < \pi/2$ is given from the boundary condition (E14) as

$$
\underset{\sim}{\gamma_1} = -\frac{2}{v_F} \exp\left[2s_\theta|\Psi(\hat{\boldsymbol{k}})|F(\sigma, z_0, \theta) \right] \int_{\sigma}^{\frac{a_c}{\sin\theta}} d\sigma' \left[-is_\mu \frac{b}{\sigma' \sin\theta} \Delta_0^* + \omega_n \underset{\sim}{\gamma_0} \right] \exp[-2s_\theta|\Psi(\hat{\boldsymbol{k}})|F(\sigma', z_0, \theta)]
$$
$$
- \left\{ \frac{s_\mu \Psi^*(\hat{\boldsymbol{k}})e^{i\phi}}{\Delta_\infty |\Psi(\hat{\boldsymbol{k}})|^2} |\omega_n| - i\frac{s_\mu \Psi^*(\hat{\boldsymbol{k}})e^{i\phi}}{|\Psi(\hat{\boldsymbol{k}})|} \frac{b}{a_c} \right\} \exp\left[2s_\theta|\Psi(\hat{\boldsymbol{k}})| \left\{ F(\sigma, z_0, \theta) - F\left(\frac{a_c}{\sin\theta}, z_0, \theta \right) \right\} \right]. \tag{E27}
$$

We respectively set the integral constants as $\sigma_0 = -a_c/\sin\theta$ and $\underset{\sim}{\sigma_0} = a_c/\sin\theta$. From the boundary condition (A9), γ_1 in $0 \leqslant \theta < \pi/2$ and $\underset{\sim}{\gamma_1}$ in $\pi/2 < \theta \leqslant \pi$ are given as

$$
\gamma_1 = \frac{2}{v_F} \exp\left[2|\Psi(\hat{\boldsymbol{k}})|F(\sigma, z_0, \theta) \right] \int_{-\frac{z_0}{\cos\theta}}^{\sigma} d\sigma' \left[-i\frac{b}{\sigma' \sin\theta} \Delta_0 - \omega_n \gamma_0 \right] \exp[-2|\Psi(\hat{\boldsymbol{k}})|F(\sigma', z_0, \theta)]
$$
$$
+ \frac{2}{v_F} \int_{-\frac{a_c}{\sin\theta}}^{-\frac{z_0}{\cos\theta}} d\sigma' \left[-i\frac{b}{\sigma' \sin\theta} \Delta_0(-z_0, \pi - \theta) - \omega_n \gamma_0 \right] \exp[2|\Psi(\hat{\boldsymbol{k}})|\{F(\sigma, z_0, \theta) - F(\sigma', -z_0, \pi - \theta)\}]
$$
$$
+ s_\theta \left\{ \frac{\Psi(\hat{\boldsymbol{k}})e^{-i\phi}}{\Delta_\infty |\Psi(\hat{\boldsymbol{k}})|^2} |\omega_n| - i\frac{\Psi(\hat{\boldsymbol{k}})e^{-i\phi}}{|\Psi(\hat{\boldsymbol{k}})|} \frac{b}{a_c} \right\} \exp\left[2|\Psi(\hat{\boldsymbol{k}})| \left\{ F(\sigma, z_0, \theta) - F\left(-\frac{a_c}{\sin\theta}, -z_0, \pi - \theta \right) \right\} \right], \tag{E28}
$$

$$
\underset{\sim}{\gamma_1} = -\frac{2}{v_F} \exp[2s_\theta|\Psi(\hat{\boldsymbol{k}})|F(\sigma, z_0, \theta)] \int_{\sigma}^{-\frac{z_0}{\cos\theta}} d\sigma' \left[-is_\mu \frac{b}{\sigma' \sin\theta} \Delta_0^* + \omega_n \underset{\sim}{\gamma_0} \right] \exp[-2s_\theta|\Psi(\hat{\boldsymbol{k}})|F(\sigma', z_0, \theta)]
$$
$$
- \frac{2}{v_F} \int_{-\frac{z_0}{\cos\theta}}^{\frac{a_c}{\sin\theta}} d\sigma' \left[-is_\mu \frac{b}{\sigma' \sin\theta} \Delta_0^*(-z_0, \pi - \theta) + \omega_n \underset{\sim}{\gamma_0} \right] \exp\left[2s_\theta|\Psi(\boldsymbol{k})|\{F(\sigma, z_0, \theta) - F(\sigma', -z_0, \pi - \theta)\} \right]
$$
$$
- s_\theta \left\{ \frac{s_\mu \Psi^*(\hat{\boldsymbol{k}})e^{i\phi}}{\Delta_\infty |\Psi(\hat{\boldsymbol{k}})|^2} |\omega_n| - i\frac{s_\mu \Psi^*(\hat{\boldsymbol{k}})e^{i\phi}}{|\Psi(\hat{\boldsymbol{k}})|} \frac{b}{a_c} \right\} \exp\left[2s_\theta|\Psi(\hat{\boldsymbol{k}})| \left\{ F(\sigma, z_0, \theta) - F\left(\frac{a_c}{\sin\theta}, -z_0, \pi - \theta \right) \right\} \right]. \tag{E29}
$$

When we take $z = 0$, $a_c \to \infty$, we obtain

$$
F\left(\sigma = -\frac{z_0}{\cos\theta}, z_0, \theta \right) = 0, \tag{E30}
$$

$$
F\left(\sigma = -\infty, z_0, \frac{\pi}{2} < \theta \leqslant \pi \right) = s_\theta F\left(\sigma = +\infty, z_0, 0 \leqslant \theta < \frac{\pi}{2} \right) = \infty. \tag{E31}
$$

As a result, γ_1 and $\underset{\sim}{\gamma}_1$ in $0 \leqslant \theta < \pi/2$ is given as

$$\gamma_1 = \frac{2}{v_F} \int_{-\infty}^{-\frac{z_0}{\cos\theta}} d\sigma' \left[-i\frac{b}{\sigma'\sin\theta} \Delta_0(-z_0, \pi - \theta) - \omega_n \gamma_0 \right] \exp[-2|\Psi(\hat{k})|F(\sigma', -z_0, \pi - \theta)], \tag{E32}$$

$$\underset{\sim}{\gamma}_1 = -\frac{2}{v_F} \int_{-\frac{z_0}{\cos\theta}}^{\infty} d\sigma' \left[-is_\mu \frac{b}{\sigma'\sin\theta} \Delta_0^* + \omega_n \underset{\sim}{\gamma}_0 \right] \exp[-2s_\theta|\Psi(\hat{k})|F(\sigma', z_0, \theta)], \tag{E33}$$

and ones in $\pi/2 \leqslant \theta < \pi$ is given as

$$\gamma_1 = \frac{2}{v_F} \int_{-\infty}^{-\frac{z_0}{\cos\theta}} d\sigma' \left[-i\frac{b}{\sigma'\sin\theta} \Delta_0 - \omega_n \gamma_0 \right] \exp\left[-2|\Psi(\hat{k})|F(\sigma', z_0, \theta) \right], \tag{E34}$$

$$\underset{\sim}{\gamma}_1 = -\frac{2}{v_F} \int_{-\frac{z_0}{\cos\theta}}^{\infty} d\sigma' \left[-is_\mu \frac{b}{\sigma'\sin\theta} \Delta_0^*(-z_0, \pi - \theta) + \omega_n \underset{\sim}{\gamma}_0 \right] \exp\left[-2s_\theta|\Psi(k)|F(\sigma', -z_0, \pi - \theta) \right]. \tag{E35}$$

We can replace z to $|z|$ due to $z = \sigma \cos\theta + z_0 > 0$. By this substitution, we can rewrite γ_1 and $\underset{\sim}{\gamma}_1$ in $0 \leqslant \theta \leqslant \pi$ as

$$\gamma_1 = \frac{2}{v_F} \int_{-\infty}^{-\frac{z_0}{\cos\theta}} d\sigma' \left[-i\frac{b}{\sigma'\sin\theta} \bar{\Delta}(\sigma') - \omega_n \gamma_0 \right] \exp\left[-2|\Psi(k)|\bar{F}(\sigma') \right], \tag{E36}$$

$$\underset{\sim}{\gamma}_1 = -\frac{2}{v_F} \int_{-\frac{z_0}{\cos\theta}}^{\infty} d\sigma' \left[-is_\mu s_\theta \frac{b}{\sigma'\sin\theta} \bar{\Delta}^*(\sigma') + \omega_n \underset{\sim}{\gamma}_0 \right] \exp\left[-2|\Psi(k)|\bar{F}(\sigma') \right], \tag{E37}$$

where we define $\bar{\Delta}$ and $\bar{F}$ as

$$\bar{\Delta}(\sigma, z_0, \hat{k}) = h(|\sigma'|\sin\theta, |\sigma'\cos\theta + z_0|)e^{i\phi}\mathrm{sign}(\sigma)\Psi(\max\{\theta, \pi - \theta\}, \phi), \tag{E38}$$

$$\bar{F}(\sigma, z_0, \hat{k}) = \int_{-\frac{z_0}{\cos\theta}}^{\sigma} \mathrm{sign}(\sigma')h(|\sigma'|\sin\theta, |\sigma'\cos\theta + z_0|)d\sigma'. \tag{E39}$$

The quasiclassical Green's functions are expanded as

$$g = \frac{1 - s_\mu \gamma \underset{\sim}{\gamma}}{1 + s_\mu \gamma \underset{\sim}{\gamma}} \simeq \frac{1 - s_\mu(\gamma_0\underset{\sim}{\gamma}_0 + \gamma_1\underset{\sim}{\gamma}_0 + \gamma_0\underset{\sim}{\gamma}_1)}{1 + s_\mu(\gamma_0\underset{\sim}{\gamma}_0 + \gamma_1\underset{\sim}{\gamma}_0 + \gamma_0\underset{\sim}{\gamma}_1)}, \tag{E40}$$

$$f = \frac{2\gamma}{1 + s_\mu \gamma \underset{\sim}{\gamma}} \simeq \frac{2\gamma_0 + 2\gamma_1}{1 + s_\mu(\gamma_0\underset{\sim}{\gamma}_0 + \gamma_1\underset{\sim}{\gamma}_0 + \gamma_0\underset{\sim}{\gamma}_1)}. \tag{E41}$$

The relation $\gamma_0\underset{\sim}{\gamma}_0 = -s_\mu s_\theta$ is important. In the case of $s_\theta = 1$, zeroth-order Green's functions diverge, whereas ones do not in the case of $s_\theta = -1$. We consider the case of $s_\theta = -1$. In this case, the first-order Green's functions are approximated as

$$g \simeq -\frac{s_\mu W}{2 + s_\mu W}, \quad f \simeq \frac{2\gamma_0 + 2\gamma_1}{2 + s_\mu W}, \tag{E42}$$

where we define

$$W(b, z_0, k) = \gamma_1\underset{\sim}{\gamma}_0 + \gamma_0\underset{\sim}{\gamma}_1 = \frac{2}{v_F} \int_{-\infty}^{\infty} d\sigma' \left[-i\frac{b}{\sigma'\sin\theta} \bar{\Delta}(\sigma')\underset{\sim}{\gamma}_0 - s_\mu \omega_n \right] \exp[-2|\Psi(k)|\bar{F}(\sigma')]. \tag{E43}$$

In the cylindrical coordinate $\boldsymbol{r} = (\rho, \Phi, z = 0)$, W is rewritten as

$$W(\rho, \Phi, z = 0, k) = -2s_\mu(i\rho CD + \omega_n C), \tag{E44}$$

where we use $b = \rho \sin(\phi - \Phi)$ and define D and C as

$$D(\rho, \Phi, k) = \frac{2}{C(\rho, \Phi, k)} \int_{-\infty}^{\infty} d\sigma' \frac{\sin(\phi - \Phi)}{\sigma'\sin\theta} h\left(|\sigma|\sin\theta, \left| \sigma\cos\theta - \rho\frac{\cos(\phi - \Phi)}{\tan\theta} \right| \right) \exp[-2|\Psi(k)|\bar{F}(\rho, \Phi, \sigma', k)] \tag{E45}$$

$$= \frac{\sin(\phi - \Phi)}{\sin\theta} \tilde{D}(\rho, \Phi, k), \tag{E46}$$

$$C(\rho, \Phi, k) = \frac{2}{v_F} \int_{-\infty}^{\infty} d\sigma' \exp[-2|\Psi(k)|\bar{F}(\rho, \Phi, \sigma', k)]. \tag{E47}$$

It is noted that $\tilde{D}$, $C > 0$ due to $h > 0$. The azimuthal component of the current density is written as

$$j_\Phi(\boldsymbol{r}) = -4|e|N_0\pi T \sum_{n=0}^\infty \int \frac{d\Omega}{4\pi} v_F \sin\theta \sin(\phi - \Phi)\mathrm{Im}g(\hat{\boldsymbol{k}}, \boldsymbol{r}, i\omega_n). \tag{E48}$$

In order to calculate the current density, we perform the sum over the Matsubara frequencies as

$$-T\sin\theta\sin(\phi-\Phi)\sum_{n=1}^\infty \mathrm{Im}g(\rho,\Phi,\boldsymbol{k},i\omega_n) = \sum_{n=1}^\infty \frac{T\sin\theta\sin(\phi-\Phi)\rho C^{-1}D}{(i\omega_n - \rho D - iC^{-1})(i\omega_n + \rho D - iC^{-1})} \tag{E49}$$

$$= \frac{C^{-1}}{4}\sin\theta\sin(\phi-\Phi)\mathrm{Re}\left[\tanh\frac{1}{2T}(-\rho D + iC^{-1})\right]$$

$$+ \frac{1}{\pi}\int_0^\infty \frac{\sin^2(\phi-\Phi)\rho C^{-1}\tilde{D}z}{\{(z+\rho D)^2 + C^{-2}\}\{(z-\rho D)^2 + C^{-2}\}}\tanh\frac{z}{2T}dz. \tag{E50}$$

The second term is bounded from above as

$$\frac{1}{\pi}\int_0^\infty \frac{\sin^2(\phi-\Phi)\rho C^{-1}\tilde{D}z}{\{(z+\rho D)^2 + C^{-2}\}\{(z-\rho D)^2 + C^{-2}\}}\tanh\frac{z}{2T}dz$$

$$\leqslant \frac{1}{\pi}\int_0^\infty \frac{\sin^2(\phi-\Phi)\rho C^{-1}\tilde{D}z}{\{(z+\rho D)^2 + C^{-2}\}\{(z-\rho D)^2 + C^{-2}\}}dz \tag{E51}$$

$$= \frac{1}{4\pi}\sin\theta\sin(\phi-\Phi)\int_{-\rho D}^{\rho D}\frac{C^{-1}}{z^2 + C^{-2}}dz = 2\sin\theta\sin(\phi-\Phi)\tan^{-1}\left(\frac{\rho D}{C^{-1}}\right). \tag{E52}$$

From this inequality, we obtain

$$-T\sin\theta\sin(\phi-\Phi)\sum_{n=1}^\infty \mathrm{Im}g(\rho,\Phi,\boldsymbol{k},i\omega_n)$$

$$\leqslant \frac{C^{-1}}{4}\sin\theta\sin(\phi-\Phi)\mathrm{Re}\left[\tanh\frac{1}{2T}\left(-\rho D + iC^{-1}\right)\right] + 2\sin\theta\sin(\phi-\Phi)\tan^{-1}\left(\frac{\rho D}{C^{-1}}\right) \tag{E53}$$

$$\simeq \sin^2(\phi-\Phi)\left[-\frac{C^{-1}}{8T} + \frac{2}{C^{-1}}\right]\rho\tilde{D} + O(\rho^2). \tag{E54}$$

Therefore, the vortex current at $\rho \ll \xi$ and $T \ll \Delta$ is bounded from above as follows:

$$j_\Phi(\rho) \leqslant 4|e|N_0\pi v_F \int \frac{d\Omega}{4\pi}\sin^2(\phi-\Phi)\left[-\frac{C^{-1}}{8T} + \frac{2}{C^{-1}}\right]\rho\tilde{D}. \tag{E55}$$

On the other hand, in the case of $s_\theta = 1$ or deep inside the SC, the current density is given by

$$j_\Phi(\rho) = 4|e|N_0\pi v_F \int \frac{d\Omega}{4\pi}\sin\theta\sin(\phi-\Phi)\frac{C^{-1}}{2}\tanh\left(\frac{\rho D}{2T}\right) \tag{E56}$$

$$\simeq 4|e|N_0\pi v_F \int \frac{d\Omega}{4\pi}\sin^2(\phi-\Phi)\frac{C^{-1}}{4T}\rho\tilde{D} + O(\rho^2), \tag{E57}$$

where N_0 is the density of state in the normal state. These equations (E55) and (E57) show that the vortex current is reversed near the surface when $s_\theta = -1$.

The LDOS is written as

$$\frac{N(E,\rho)}{N_0} = -\lim_{\delta\to 0}\int \frac{d\Omega}{4\pi}\mathrm{Re}g(\boldsymbol{k}, \boldsymbol{r}, E + i\delta). \tag{E58}$$

From Eq. (E42), the LDOS is calculated as

$$\frac{N(E,\rho)}{N_0} = -\lim_{\delta\to 0}\int \frac{d\Omega}{4\pi}\mathrm{Re}\frac{\rho D + E + i\delta}{iC^{-1} - \rho D - E - i\delta} \tag{E59}$$

$$= \int \frac{d\Omega}{4\pi}\frac{(\rho D + E)^2}{(\rho D + E)^2 + C^{-2}} \leqslant 1. \tag{E60}$$

Therefore, the LDOS is suppressed significantly at $\rho \ll \xi$ and $E \ll |\Delta|$ and equals zero especially at $\rho = 0$ and $E = 0$. These results are consistent with numerical results for the p_z-wave SC in the main texts.

[1] A. Di Bernardo, Z. Salman, X. L. Wang, M. Amado, M. Egilmez, M. G. Flokstra, A. Suter, S. L. Lee, J. H. Zhao, T. Prokscha, E. Morenzoni, M. G. Blamire, J. Linder, and J. W. A. Robinson, Intrinsic Paramagnetic Meissner Effect Due to s-Wave Odd-Frequency Superconductivity, Phys. Rev. X **5**, 041021 (2015).

[2] J. A. Krieger, A. Pertsova, S. R. Giblin, M. Döbeli, T. Prokscha, C. W. Schneider, A. Suter, T. Hesjedal, A. V. Balatsky, and Z. Salman, Proximity-Induced Odd-Frequency Superconductivity in a Topological Insulator, Phys. Rev. Lett. **125**, 026802 (2020).

[3] V. L. Berezinskii, New model of the anisotropic phase of superfluid He^3, Pis'ma Zh. Eksp. Teor. Fiz. **20**, 628 (1974) [Sov. Phys. JETP Lett. **20**, 287 (1974)].

[4] A. Balatsky and E. Abrahams, New class of singlet superconductors which break the time reversal and parity, Phys. Rev. B **45**, 13125 (1992).

[5] J. Linder and A. V. Balatsky, Odd-frequency superconductivity, Rev. Mod. Phys. **91**, 045005 (2019).

[6] Y. Asano, A. A. Golubov, Ya. V. Fominov, and Y. Tanaka, Unconventional Surface Impedance of a Normal-Metal Film Covering a Spin-Triplet Superconductor Due to Odd-Frequency Cooper Pairs, Phys. Rev. Lett. **107**, 087001 (2011).

[7] T. Yokoyama, Y. Tanaka, and N. Nagaosa, Anomalous Meissner Effect in a Normal-Metal–Superconductor Junction with a Spin-Active Interface, Phys. Rev. Lett. **106**, 246601 (2011).

[8] S. Higashitani, H. Takeuchi, S. Matsuo, Y. Nagato, and K. Nagai, Magnetic Response of Odd-Frequency s-Wave Cooper Pairs in a Superfluid Proximity System, Phys. Rev. Lett. **110**, 175301 (2013).

[9] S. Higashitani, Odd-frequency pairing effect on the superfluid density and the pauli spin susceptibility in spatially nonuniform spin-singlet superconductors, Phys. Rev. B **89**, 184505 (2014).

[10] S.-I. Suzuki and Y. Asano, Paramagnetic instability of small topological superconductors, Phys. Rev. B **89**, 184508 (2014).

[11] S.-I. Suzuki and Y. Asano, Effects of surface roughness on the paramagnetic response of small unconventional superconductors, Phys. Rev. B **91**, 214510 (2015).

[12] Y. Asano and A. Sasaki, Odd-frequency cooper pairs in two-band superconductors and their magnetic response, Phys. Rev. B **92**, 224508 (2015).

[13] Y. Tanaka and S. Kashiwaya, Theory of Tunneling Spectroscopy of d-Wave Superconductors, Phys. Rev. Lett. **74**, 3451 (1995).

[14] Y. Tanaka, Y. Asano, A. A. Golubov, and S. Kashiwaya, Anomalous features of the proximity effect in triplet superconductors, Phys. Rev. B **72**, 140503(R) (2005).

[15] Y. Tanaka and A. A. Golubov, Theory of the Proximity Effect in Junctions with Unconventional Superconductors, Phys. Rev. Lett. **98**, 037003 (2007).

[16] M. Eschrig and T. Löfwander, Triplet supercurrents in clean and disordered half-metallic ferromagnets, Nat. Phys. **4**, 138 (2008).

[17] S.-I. Suzuki and Y. Asano, Spontaneous edge current in a small chiral superconductor with a rough surface, Phys. Rev. B **94**, 155302 (2016).

[18] A. A. Golubov, M. Yu. Kupriyanov, and M. M. Khapaev, Abrikosov vortices in sf bilayers, JETP Lett. **104**, 847 (2016).

[19] Y. Asano, Y. Tanaka, and A. A. Golubov, Josephson Effect due to Odd-Frequency Pairs in Diffusive Half Metals, Phys. Rev. Lett. **98**, 107002 (2007).

[20] Y. Tanaka, M. Sato, and N. Nagaosa, Symmetry and topology in superconductors -odd-frequency pairing and edge states-, J. Phys. Soc. Jpn. **81**, 011013 (2012).

[21] S.-I. Suzuki, T. Hirai, M. Eschrig, and Y. Tanaka, Anomalous inverse proximity effect in unconventional superconductor junctions, Phys. Rev. Res. **3**, 043148 (2021).

[22] M. Rogers, A. Walton, M. G. Flokstra, A. Ma'Mari, R. Stewart, S. L. Lee, T. Prokscha, A. J. Caruana, C. J. Kinane, S. Langridge *et al.*, Spin-singlet to triplet cooper pair converter interface, Commun. Phys. **4**, 69 (2021).

[23] T. Yokoyama, Y. Tanaka, and A. A. Golubov, Theory of pairing symmetry inside the Abrikosov vortex core, Phys. Rev. B **78**, 012508 (2008).

[24] Y. Tanuma, N. Hayashi, Y. Tanaka, and A. A. Golubov, Model for Vortex-Core Tunneling Spectroscopy of Chiral p-Wave Superconductors via Odd-Frequency Pairing States, Phys. Rev. Lett. **102**, 117003 (2009).

[25] Y. Tanaka, Y. Tanuma, and A. A. Golubov, Odd-frequency pairing in normal-metal/superconductor junctions, Phys. Rev. B **76**, 054522 (2007).

[26] M. Eschrig, T. Löfwander, T. Champel, J. C. Cuevas, J. Kopu, and G. Schön, Symmetries of pairing correlations in superconductor–ferromagnet nanostructures, J. Low Temp. Phys. **147**, 457 (2007).

[27] J. Hara and K. Nagai, A polar state in a slab as a soluble model of p-wave Fermi superfluid in finite geometry, Prog. Theor. Phys. **76**, 1237 (1986).

[28] The vortex shadow effect [59–62] was discussed. However, odd-ω pairs are not in the same location.

[29] S. Ran, C. Eckberg, Q.-P. Ding, Y. Furukawa, T. Metz, S. R. Saha, I.-L. Liu, M. Zic, H. Kim, J. Paglione, and N. P. Butch, Nearly ferromagnetic spin-triplet superconductivity, Science **365**, 684 (2019).

[30] A. Pustogow, Y. Luo, A. Chronister, Y.-S. Su, D. A. Sokolov, F. Jerzembeck, A. P. Mackenzie, C. W. Hicks, N. Kikugawa, S. Raghu *et al.*, Constraints on the superconducting order parameter in Sr_2RuO_4 from oxygen-17 nuclear magnetic resonance, Nature (London) **574**, 72 (2019).

[31] H. G. Suh, H. Menke, P. M. R. Brydon, C. Timm, A. Ramires, and D. F. Agterberg, Stabilizing even-parity chiral superconductivity in Sr_2RuO_4, Phys. Rev. Res. **2**, 032023(R) (2020).

[32] V. Grinenko, S. Ghosh, R. Sarkar, J.-C. Orain, A. Nikitin, M. Elender, D. Das, Z. Guguchia, F. Brückner, M. E. Barber *et al.*, Split superconducting and time-reversal symmetry-breaking transitions in Sr_2RuO_4 under stress, Nat. Phys. **17**, 748 (2021).

[33] V. Grinenko, D. Das, R. Gupta, B. Zinkl, N. Kikugawa, Y. Maeno, C. W. Hicks, H.-H. Klauss, M. Sigrist, and R. Khasanov, Unsplit superconducting and time reversal symmetry breaking transitions in Sr_2RuO_4 under hydrostatic pressure and disorder, Nat. Commun. **12**, 3920 (2021).

[34] S. Kobayashi, Y. Tanaka, and M. Sato, Fragile surface zero-energy flat bands in three-dimensional chiral superconductors, Phys. Rev. B **92**, 214514 (2015).

[35] S. Tamura, S. Kobayashi, L. Bo, and Y. Tanaka, Theory of surface Andreev bound states and tunneling spectroscopy in three-dimensional chiral superconductors, Phys. Rev. B **95**, 104511 (2017).

[36] S.-I. Suzuki, M. Sato, and Y. Tanaka, Identifying possible pairing states in Sr_2RuO_4 by tunneling spectroscopy, Phys. Rev. B **101**, 054505 (2020).

[37] S.-I. Suzuki, S. Ikegaya, and A. A Golubov, Destruction of surface states of $(d_{zx} + id_{yz})$-wave superconductor by surface roughness: Application to Sr_2RuO_4, Phys. Rev. Res. **4**, L042020 (2022)

[38] H. F. Hess, R. B. Robinson, R. C. Dynes, J. M. Valles, and J. V. Waszczak, Scanning-Tunneling-Microscope Observation of the Abrikosov Flux Lattice and the Density of States near and inside a Fluxoid, Phys. Rev. Lett. **62**, 214 (1989).

[39] J. R. Kirtley and J. P. Wikswo Jr, Scanning squid microscopy, Annu. Rev. Mater. Sci. **29**, 117 (1999).

[40] F. S. Wells, A. V. Pan, X. R. Wang, S. A. Fedoseev, and H. Hilgenkamp, Analysis of low-field isotropic vortex glass containing vortex groups in $YBa_2Cu_3O_{7-x}$ thin films visualized by scanning SQUID microscopy, Sci. Rep. **5**, 8677 (2015).

[41] C. Caroli, P.G. De Gennes, and J. Matricon, Bound Fermion states on a vortex line in a type II superconductor, Phys. Lett. **9**, 307 (1964).

[42] F. Gygi and M. Schlüter, Self-consistent electronic structure of a vortex line in a type-II superconductor, Phys. Rev. B **43**, 7609 (1991).

[43] L. Kramer and W. Pesch, Core structure and low-energy spectrum of isolated vortex lines in clean superconductors at $T \ll T_c$, Z. Phys. **269**, 59 (1974).

[44] Y. Nagai, Y. Ueno, Y. Kato, and N. Hayashi, Analytical formulation of the local density of states around a vortex core in unconventional superconductors, J. Phys. Soc. Jpn. **75**, 104701 (2006).

[45] Y. Nagai and Y. Kato, Quasiparticle bound states around fractional vortices in s-wave superconductor, J. Phys. Soc. Jpn. **88**, 054707 (2019).

[46] G. Eilenberger, Transformation of Gorkov's equation for type II superconductors into transport-like equations, Z. Phys. **214**, 195 (1968).

[47] G. Eilenberger and H. Büttner, The structure of single vortices in type II superconductors, Z. Phys. **224**, 335 (1969).

[48] A. Larkin and Y. N. Ovchinnikov, Quasiclassical method in the theory of superconductivity, Zh. Eksp. Teor. Fiz. **55**, 2262 (1968) [Sov. Phys. JETP **28**, 1200 (1969)].

[49] N. Schopohl and K. Maki, Quasiparticle spectrum around a vortex line in a d-wave superconductor, Phys. Rev. B **52**, 490 (1995).

[50] N. Schopohl, Transformation of the Eilenberger equations of superconductivity to a scalar Riccati equation, arXiv:cond-mat/9804064.

[51] When there are ABSs forming a flat band, it is important to obtain the self-consistent solutions. Non-self-consistent simulations under a magnetic field such as the linear response theory often give overstated results because the LDOS has a singularity at the zero energy (see, for example, Ref. [9]).

[52] Since the electromagnetism is a three dimensional problem, we need to solve the magnetic field in three dimensions. The magnetic-field distribution is not determined locally. We need to integrate the current density in a whole system.

[53] S. Higashitani, Spin current as a manifestation of surface odd-frequency pairing in superfluid 3He, J. Phys. Soc. Jpn. **83**, 075002 (2014).

[54] At a surface of an SC, the incoming and outgoing quasiparticles interfere. These two quasiparticles feel, in general, different pair potentials depending on the momentum: $\Delta(k_z, \boldsymbol{k}_\parallel)$ and $\Delta(-k_z, \boldsymbol{k}_\parallel)$ where the surface is perpendicular to the z axis. In the p_z-wave SC, the phase difference between these two pair potentials is π: $\Delta(k_z, \boldsymbol{k}_\parallel) = -\Delta(-k_z, \boldsymbol{k}_\parallel)$. The π-phase shift results in forming the surface bound state at the zero energy.

[55] C.-R. Hu, Midgap Surface States as a Novel Signature for d_{xa}^2-x_b^2-Wave Superconductivity, Phys. Rev. Lett. **72**, 1526 (1994).

[56] S. Kashiwaya and Y. Tanaka, Tunnelling effects on surface bound states in unconventional superconductors, Rep. Prog. Phys. **63**, 1641 (2000).

[57] M. Sato, Y. Tanaka, Keiji Yada, and T. Yokoyama, Topology of Andreev bound states with flat dispersion, Phys. Rev. B **83**, 224511 (2011).

[58] The energy levels for the CdGM modes are given by $E = \pm(n - 1/2)\Delta_\infty^2/E_F$. In the quasiclassical regime, the lowest CdGM mode seem to sit at $E = 0$ because $\Delta/E_F \ll 1$ is assumed in the quasiclassical theory.

[59] S. Graser, C. Iniotakis, T. Dahm, and N. Schopohl, Shadow on the Wall Cast by an Abrikosov Vortex, Phys. Rev. Lett. **93**, 247001 (2004).

[60] T. Yokoyama, C. Iniotakis, Y. Tanaka, and M. Sigrist, Chirality Sensitive Effect on Surface States in Chiral p-Wave Superconductors, Phys. Rev. Lett. **100**, 177002 (2008).

[61] M. A. Silaev, Electronic structure of edge and vortex states in chiral mesoscopic superconductor, JETP Lett. **87**, 441 (2008).

[62] M. A. Silaev, T. Yokoyama, J. Linder, Y. Tanaka, and A. Sudbø, Tunneling conductance and local density of states in time-reversal symmetry breaking superconductors under the influence of an external magnetic field, Phys. Rev. B **79**, 054508 (2009).